Shortwave Radiative Impacts from Aerosol Effects on Marine Shallow Cumuli

PAQUITA ZUIDEMA

Rosenstiel School of Marine and Atmospheric Sciences, University of Miami, Miami, Florida

HUIWEN XUE

Department of Atmospheric Sciences, School of Physics, Peking University, Beijing, China

GRAHAM FEINGOLD

NOAA/Earth System Research Laboratory, Boulder, Colorado

(Manuscript received 5 March 2007, in final form 5 November 2007)

ABSTRACT

The net shortwave radiative impact of aerosol on simulations of two shallow marine cloud cases is investigated using a Monte Carlo radiative transfer model. For a shallow cumulus case, increased aerosol concentrations are associated not only with smaller droplet sizes but also reduced cloud fractions and cloud dimensions, a result of evaporation-induced mixing and a lack of precipitation. Three-dimensional radiative transfer (3DRT) effects alter the fluxes by 10%–20% from values calculated using the independent column approximation for these simulations. The first (Twomey) aerosol indirect effect is dominant but the decreased cloud fraction reduces the magnitude of the shortwave cloud forcing substantially. The 3DRT effects slightly decrease the sensitivity of the cloud albedo to changes in droplet size under an overhead sun for the two ranges of cloud liquid water paths examined, but not strongly so. A popular two-stream radiative transfer approximation to the cloud susceptibility overestimates the more directly calculated values for the low liquid-water-path clouds within pristine aerosol conditions by a factor of 2 despite performing well otherwise, suggesting caution in its application to the cloud albedos within broken cloud fields. An evaluation of the influence of cloud susceptibility and cloud fraction changes to a "domain" area-weighted cloud susceptibility found that the domain cloud albedo is more likely to increase under aerosol loading at intermediate aerosol concentrations than under the most pristine conditions, contrary to traditional expectations.

The second simulation (cumulus penetrating into stratus) is characterized by higher cloud fractions and more precipitation. This case has two regimes: a clean, precipitating regime where cloud fraction increases with increasing aerosol, and a more polluted regime where cloud fraction decreases with increasing aerosol. For this case the domain-mean cloud albedo increases steadily with aerosol loading under clean conditions, but increases only slightly after the cloud coverage decreases. Three-dimensional radiative transfer effects are mostly negligible for this case. Both sets of simulations suggest that aerosol-induced cloud fraction changes must be considered in tandem with the Twomey effect for clouds of small dimensions when assessing the net radiative impact, because both effects are drop size dependent and radiatively significant.

1. Introduction

The radiative forcing of climate by shallow cumulus clouds is significant, given a 25% frequency of occurrence and 12% cloud fraction over ocean as estimated by human observers (Norris 1998). The cloud response to aerosol is climatically important (e.g., Lohmann and Feichter 2005), but many aerosol indirect effects (AIEs) remain poorly characterized. Large-scale surface- and satellite-based observational studies provide detailed information useful for quantifying the net radiative effect; however, such studies show apparently conflicting results. For example, an increase in cloud fraction and cloud liquid water path in the presence of aerosol has been observed (e.g., Kaufman et al. 2005; Norris 2001) but other satellite remote sensing studies show that cloud fractions and liquid water paths can

Corresponding author address: Paquita Zuidema, RSMAS/MPO, University of Miami, 4600 Rickenbacker Causeway, Miami, FL 33149-1098.
E-mail: pzuidema@rsmas.miami.edu

DOI: 10.1175/2007JAS2447.1

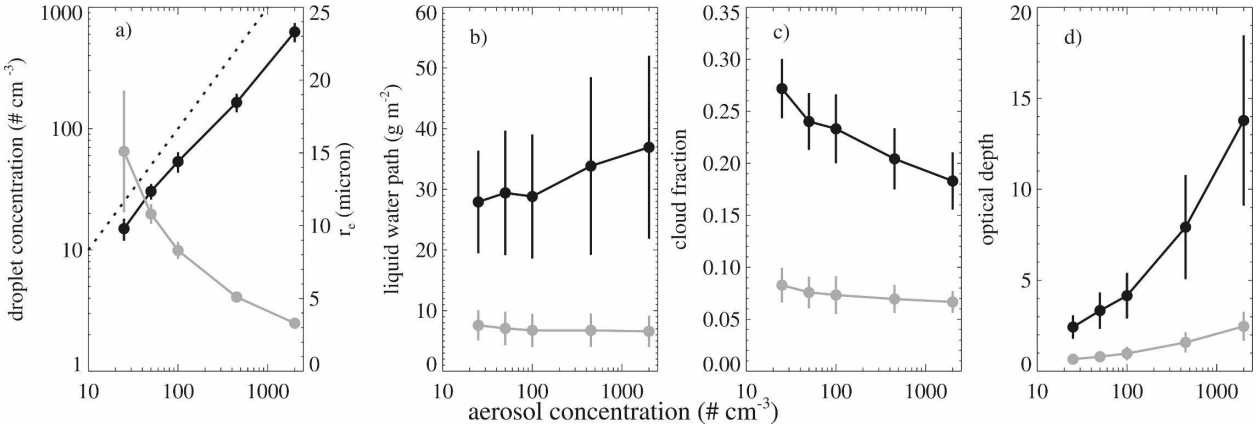

FIG. 1. (a) Cloud droplet concentration (black line; left-hand axis) and cloud effective radius (gray line; right-hand axis) as a function of aerosol concentration. (b) Cloud (black) and domain-averaged (gray) LWP. (c) Cloud fraction using optical depths >0.001 (black; based on $Q_{ext} = 2$) and LWPs >10 g m^{-2} (gray). (d) Cloud (black) and domain-averaged (gray) optical depth. All values (except aerosol concentration) are shown as the mean of the last 4 h of each simulation, with bars indicating ±1 std dev. Cloudy columns are defined by cloud optical depth exceeding 0.001, excepting (c). This figure summarizes the BOMEX results shown in XF06.

decrease as well as increase (Han et al. 2002; Matheson et al. 2005), or just decrease (Matsui et al. 2006) with increased aerosol concentrations. The discrepancies may reflect effects from meteorology as well as aerosol. Particularly for shallow marine cumuli, however, the challenges in the satellite remote sensing of these clouds of small dimensions, variable cloud optical depths, and low cloud-top heights (e.g., Genkova et al. 2007; Wielicki and Parker 1992; Zhao and Girolamo 2006) also confuse the interpretation of results. Finally, it is also important to differentiate between the correlations shown in these studies and the more elusive causal relationships.

Another approach is to use observed or modeled properties of polluted and pristine clouds and model the radiative change associated with particular aerosol indirect effects. One such study found that soot-polluted clouds were ultimately less reflective than pristine clouds despite a smaller droplet size (and similar cloud liquid water paths) because of reduced cloud coverage (McFarquhar et al. 2004). The authors attributed this to the absorption of solar radiation by soot, also known as the semidirect effect (Ackerman et al. 2000).

An aerosol–cloud interaction wherein increased (nonabsorbing) aerosol concentrations not only increased cloud optical depths but also decreased cloud fractions and decreased cloud horizontal dimensions has been identified by Xue and Feingold (2006, hereafter XF06) and Jiang et al. (2006). The simulations exhibit a positive evaporation–entrainment feedback whereby latent cooling associated with small-drop evaporation strengthens a horizontal buoyancy gradient that fosters more mixing of dry air into the cloud, leading to more evaporation. Simulations from XF06 done at different aerosol concentrations are shown in Fig. 1. Drizzle suppression is evident as increased cloud liquid water paths at the higher aerosol concentrations (Fig. 1b), but even at the lowest aerosol concentration only 10% of the clouds are drizzling (and only toward the end of the simulation). The hypothesized increase in cloud fraction (Albrecht 1989) is not evident in these simulations.

Similar simulations of stratiform cloud overlying cumulus (Xue et al. 2007, hereafter XFS07) are briefly summarized in Fig. 2. These show a more complex response to aerosol; while increased aerosol loading under clean conditions increases cloud fraction, at higher aerosol number mixing ratios ($>N_a$ = 100 mg^{-1}, i.e., roughly equivalent to 100 cm^{-3}), increases in aerosol result in a decrease in cloud fraction. Both the cloud and domain-mean liquid water paths decrease monotonically with increased aerosol loading. Despite the decrease in liquid water paths, the cloud and domain-averaged optical depths increase monotonically with N_a.

These simulations raise the question of the relative importance on the radiative forcing and climate of the aerosol effect on the cloud microphysics, versus the aerosol effect(s) on cloud fraction, size, and morphology (the macroscale properties). The cloud macrophysical aspects have received less attention than the microphysical aspect but have relevance for both climate modeling and interpretation of satellite data. For both the XF06 and XFS07 simulations, increases in aerosol are associated not only with changes in cloud fraction but also in cloud morphology, with clouds be-

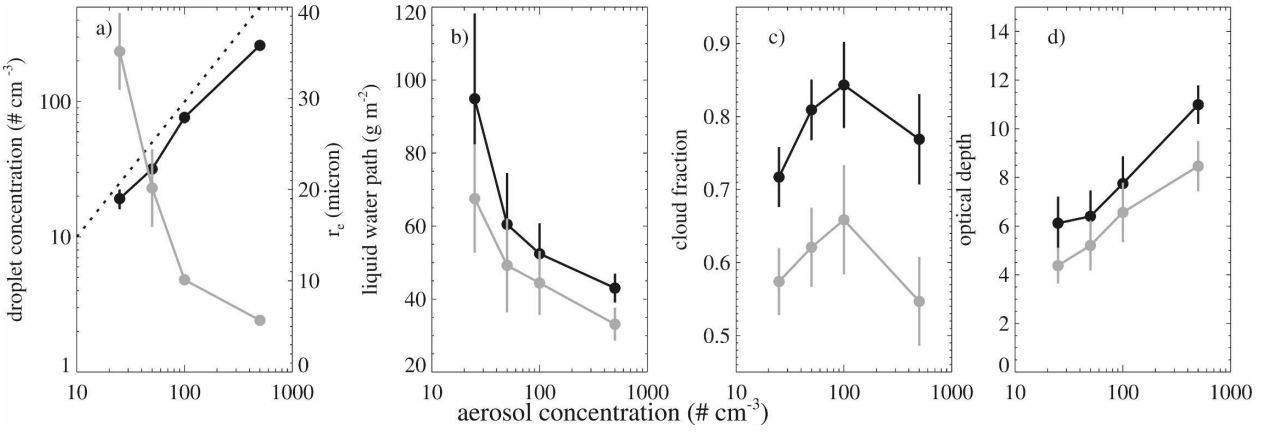

FIG. 2. (a) Cloud droplet concentration (black line; left-hand axis) and cloud effective radius (gray line; right-hand axis) as a function of aerosol concentration. (b) Cloud (black) and domain-averaged (gray) LWP. (c) Cloud fraction using optical depths >0.1 (black; based on $Q_{ext} = 2$) and LWPs >10 g m^{-2} (gray). (d) Cloud (black) and domain-averaged (gray) optical depth. All values (except aerosol concentration) are shown as the mean of the last 4 h of each simulation, with bars indicating ±1 std dev. Cloudy columns are defined by cloud optical depth exceeding 0.1, excepting (c). This figure summarizes the ATEX results shown in XFS07.

coming smaller but at times more numerous at the higher aerosol concentrations. Most of the clouds have horizontal dimensions less than 1 km, consistent with observations of trade wind cumuli (Zhao and Di Girolamo 2007), implying that three-dimensional radiative transfer (3DRT) effects are potentially important; horizontal photon transport can override the explicit connection of the shortwave radiation field to the underlying cloud microphysics. The net cloud radiative impact from the aerosol indirect effects is not intuitively obvious without a full radiative transfer calculation.

A useful measure of a cloud's sensitivity to modification by aerosol is the cloud susceptibility S (Platnick and Twomey 1994):

$$S = \left.\frac{\partial A_{\mathrm{cld}}}{\partial N_d}\right|_{\mathrm{lwc},h\ldots}, \tag{1}$$

where N_d is the cloud droplet number concentration, A_{cld} refers to the broadband cloud albedo, and all other cloud properties such as liquid water content, cloud depth, and cloud droplet size distribution width are assumed held constant. The cloud susceptibility S has been studied analytically to further understand the cloud radiative response to modification by aerosol (e.g., Feingold et al. 1997; Pincus and Baker 1994). In addition, cloud susceptibility can be assessed from satellite reflectance data (Platnick and Twomey 1994) using a two-stream approximation to S under conservative scattering (Bohren 1980), as

$$S_o \sim \frac{A_{\mathrm{cld}}(1 - A_{\mathrm{cld}})}{3N_d}, \tag{2}$$

although accurate values of N_d are difficult to obtain. Cloud susceptibility (S) is also potentially impacted by 3DRT effects; because of its usefulness both conceptually and as applied to satellite data, it is of interest to determine the extent of the 3DRT effects, both on S and S_o.

The first question this study seeks to address is the following: How does aerosol affect the cloud- and domain-mean albedo for these cases; that is, what is the overall radiative forcing associated with the microphysical and macroscale responses outlined above? The second question is this: Instead of utilizing realistic radiative transfer, could a computationally cheaper approximate radiative transfer calculation suffice in these examples? The third question is this: even if three-dimensional radiative transfer effects are significant for the albedo, is the change in albedo with droplet number concentration (S) equally affected by 3DRT effects? Can S still be usefully approximated using S_o for these clouds of small dimensions?

Below we examine two independent sets of simulations to strive for breadth in our findings, but emphasize that the results still only apply to these simulations. The radiative transfer calculations are purely a postprocessing effort, with no attempt made to incorporate radiative feedbacks into the simulations themselves. Results based on the XF06 simulations are presented first, and with more detail. The model output from the XF06 simulations is described in the next section along with the aerosol and cloud radiative representation, and the 3DRT model. Thereafter we show the mean top-of-domain albedo and fluxes for both the full (cloud + aerosol) field and for the cloud properties alone. Section 3b discusses the susceptibility of both the clouds-

only and the area-weighted domain-mean cloudy region for the XF06 simulation. Section 4 extends the findings based on the XF06 simulations to the XFS07 cases, highlighting similarities and differences.

2. Data

a. Large-eddy simulation

The five cloud simulations were performed with aerosol concentrations (N_a) of 25, 50, 100, 450, and 2000 mg^{-1}; here the units are treated identically to cm^{-3}. These included the same simulations used by XF06 and an additional one at $N_a = 100\ mg^{-1}$. The horizontal domain size of the simulations was $6.4 \times 6.4\ km^2$, with a vertical extent of 3.0 km and horizontal and vertical grid spacings of 100 and 40 m, respectively. The model dynamics were represented by an anelastic model described by Stevens et al. (1999). The simulations were based on a mean sounding from the Barbados Oceanographic and Meteorology Experiment (BOMEX; Holland and Rasmusson 1973). The simulations were similar to those done for the fourth intercomparison study of the Global Water and Energy Experiment Cloud System Studies Working Group 1 (Siebesma et al. 2003), but did not consider radiative effects and large-scale forcings.

The simulated cloud fields contained a range of cloud fractions, depths, and sizes that reflected both the internal dynamics and the aerosol response. Model output was sampled every 5 min over the course of a 4-h simulation. The mean radiative response was therefore calculated by performing a radiative transfer calculation on each of 48 individual cloud field realizations at each aerosol concentration, and computing the mean value and standard deviation from these. In practice, the cloud lifetimes of approximately 20 min (Jiang et al. 2006) provided an estimate of the autocorrelation scale consistent with what was apparent from a time series of the domain-mean cloud optical depths, and implied approximately 12 independent cloud field realizations per simulation. The domain-averaged or cloud-fraction-weighted cloud optical depth did increase with increasing aerosol concentration (Fig. 1d). This implied that the domain-mean cloudy albedo would only decrease under increased aerosol loading if three-dimensional radiative transfer effects associated with macroscale responses reduced the albedo more than the albedo increased with domain-mean cloud optical depth.

b. Aerosol

Aerosol properties were held constant in time and space for each simulation, with no sources or sinks. Their activation to cloud droplets was based on the calculated supersaturation and Kohler theory for ammonium sulfate, with the total droplet number concentration not allowed to exceed the total aerosol concentration. The XF06 lognormal aerosol distributions had a mean geometric radius of 0.1 μm and a geometric standard deviation of 1.5, corresponding to an effective radius of 0.15 μm. No giant cloud condensation nuclei were included. For the purposes of radiative transfer calculations, a particle density of 1.7 g cm^{-3} (Kiehl and Briegleb 1993) was assumed along with a hygroscopic growth factor of 1.7 (Charlson et al. 1992; Seinfeld and Pandis 1998). This accounted for the growth in particle size due to uptake of water vapor and may be an overestimate for ammonium sulfate (Kiehl and Briegleb 1993). In reality, particle growth varies as a function of relative humidity so that there is a continuum from dry aerosol to humidified haze particles, and finally cloud droplets as the relative humidity increases and eventually reaches saturation (Charlson et al. 2007; Koren et al. 2007). We made no attempt to account for these effects. A complex index of refraction of (1.53, 0.0) (Seinfeld and Pandis 1998) was used, for a single-scattering albedo of 1.0 or no solar absorption. The scattering phase function and volume extinction coefficient were determined through a Mie integration following Kiehl and Briegleb (1993).

The aerosol concentrations (N_a) of 25, 50, 100, 450, and 2000 cm^{-3} were distributed uniformly over the model vertical extent of 3 km, approximately consistent with the height of the trade wind inversion (Rauber et al. 2007; Zhao and Girolamo 2006). The corresponding optical depths of 0.00765, 0.0153, 0.0306, 0.1377, and 0.612 straddled satellite-retrieved aerosol optical depths for marine shallow cumulus regions ranging between 0.02 to 0.24 with a mean of 0.085 (Kaufman et al. 2005). The calculated asymmetry parameter g value of 0.62 was intermediate to the values of 0.52 and 0.69 used by Charlson et al. (1992) and Kiehl and Briegleb (1993) respectively. The direct radiative effect of aerosol was only accounted for in cloud-free areas, with the aerosol assumed to be embedded within a cloud droplet otherwise. Unactivated interstitial particles were ignored.

c. Radiative transfer model

The radiative transfer model is the community Monte Carlo (MC) model developed under the auspices of the Intercomparison of Three-Dimensional Radiative Transfer Codes project (Cahalan et al. 2005). This model, released in July 2006, has been tested against the other intercomparison project cases, while this study represented one of the model's first research

applications. The radiative transfer calculation was monochromatic and a wavelength of 0.64 μm was chosen for this study. Boundary conditions were periodic and a Lambertian surface albedo of 0.03 was assumed (thus no sun glint). Calculations were done for an overhead sun and at a solar zenith angle (SZA) of 60°; these two angles encompass the range of 3DRT effects.[1] Rayleigh scattering was not included, but this has no impact on the cloud radiative forcing or susceptibility calculations. Shortwave broadband values were estimated using a top-of-domain 0.64-μm irradiance of 1622 W m^{-2} μm^{-1}, a broadband solar flux of 1370 W m^{-2}, and a broadband gaseous attenuation of 20%, following McFarquhar et al. (2004). An independent column approximation (ICA) calculation was also done by disallowing horizontal photon transport, forcing photons to remain within their cloud vertical column of entry. Cloud geometry and internal optical variations were still maintained.

The volume extinction coefficient calculation was based on the full drop size information over 33 drop size bins for the lowest N_a BOMEX simulation (1.56 μm $\leq$ radius $\leq$ 3.2 mm) and 25 drop size bins for all the other BOMEX cases (1.56 μm $\leq$ radius $\leq$ 0.5 mm). All of the XFS07 simulations relied on 33 drop size bins. Several experiments were done to evaluate how much of the drop size information was necessary to accurately calculate the remaining radiative properties, namely the extinction efficiency $Q_{\text{ext}}(r)$, the single-scattering albedo $\omega(r)$, and the Mie scattering phase function $P(r)$. These three parameters only vary with the drop size and are independent of the water mass; the optical depth and volume extinction coefficient calculation always invoked a full summation over all the drops within each grid cell and were done consistently for each cloud field. Columns with optical depths greater than 0.001 constituted a cloud for this study. This definition acknowledged the radiative impact of even small liquid water amounts, and differed from that of XF06, who used a liquid water path (LWP) threshold of 10 g m^{-2} to define cloud. Mean cloud fractions for all N_a concentrations differ strongly between the two definitions (22.7% versus 7.4%). Not only is there a large percentage of low liquid water clouds, but these dissipate preferentially as N_a increases (Fig. 1c).

The first and simplest "default" calculations assumed an $\omega(r)$ of 1.0, a $Q_{\text{ext}}(r)$ of 2, and a Mie scattering phase function appropriate for an effective radius r_e of 10 μm, $P(r = r_e = 10\mu\text{m})$. Subsequent calculations used more realistic radiative property estimates. These included calculating values for ω, Q_{ext}, and P appropriate to the mean drop size associated with each N_a (see Fig. 1a), and, most explicitly, that corresponded to each grid cell's r_e.

The domain-average albedo differences calculated using individual gridcell ω, Q_{ext}, and P values; and ω, Q_{ext}, and P values based on the mean r_e for a given N_a were negligible. In contrast, the albedos calculated using ω, Q_{ext}, and P values appropriate for the mean r_e at each N_a were 5%–10% relatively brighter at the two most polluted simulations (N_a = 450 and 2000 mg^{-1}) when compared to the initial "default" calculation, possibly because of a sharp increase in the value of Q_{ext} for those drop sizes. Albedo values were unaffected by these ω, Q_{ext}, and P variations at the other three aerosol concentrations. On the basis of these experiments, we elected to use the single-scattering albedo, Mie extinction efficiency, and Mie scattering phase function appropriate for r_e of 3.3 and 5.1 μm for N_a = 450 and 2000 mg^{-1}, respectively, and otherwise relied on the default calculations.

A total of 10^6 photons were applied to each calculation: these provide domain-mean and column fluxes accurate to ~0.1% and 6% respectively. The cloud-only radiative contribution was estimated by subtracting the area-weighted ICA-calculated aerosol radiative values from the domain-mean value. This was more accurate than relying on the cloudy-column fluxes, and retained some of the 3DRT cloud influences on the aerosol albedo (e.g., Wen et al. 2006, 2007), though neglected the contribution from enhanced molecular scattering.

3. Results for shallow cumulus: BOMEX simulations

a. Top-of-domain radiative forcing

Figure 3 shows the domain-mean albedo for the MC and ICA calculations, for overhead sun and at a SZA of 60°. Contributions from both cloud and aerosol (and the surface) are included. The aerosol-only contribution is also shown; this still includes the surface and is inferred from the cloud-free pixels within the ICA calculation, so that any 3DRT cloud brightening of the aerosol albedo is not included. Under overhead sun the MC domain-average albedo is less than that from the ICA calculation at low N_a (~10% relative difference),

[1] Radiative smoothing, whereby photons travel horizontally toward optically thinner regions, is most pronounced under overhead sun. At larger solar zenith angles cloud fields become more reflective partly because the cloud effective area increases when the cloud sides become exposed to the sun, and because of radiative roughening, a primarily single-scattering phenomenon whereby cloud bumps help increase upward reflection. Modeling studies have shown that these effects can be pronounced for strongly broken cloud fields (e.g., Kite 1987; Pincus et al. 2005; Várnai 2000; Welch and Wielicki 1984).

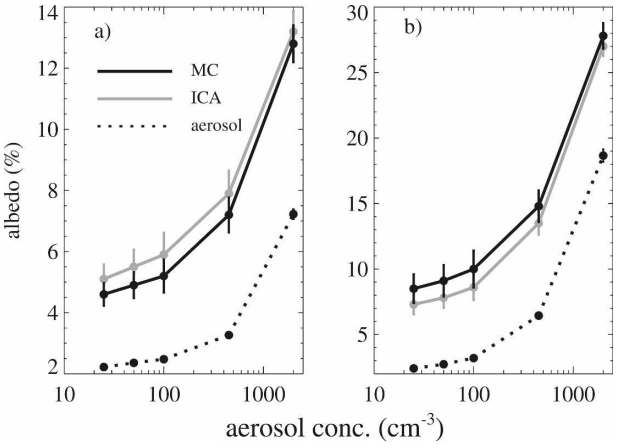

FIG. 3. The MC (black), ICA (gray) domain-mean spectral albedo (cloud and aerosol), and the area-weighted aerosol-only albedo (dotted line) as a function of aerosol concentration for (a) overhead sun and (b) a SZA of 60° for the BOMEX simulations. Values shown are the averages of the last 4 h of the simulation ±1 std dev. Note the different scales for (a) and (b).

even though two-thirds of the domain is cloud free (Fig. 1c). At the greater solar zenith angle, the MC domain-mean albedo exceeds the ICA albedo by a ~10% relative difference at the lower N_a values. At the highest N_a more than one-half of the domain-mean albedo is accounted for by just the aerosol.

The albedo values are shown translated into spectral and broadband radiative forcing values in Fig. 4. These values are calculated as the difference between the net cloud + aerosol domain fluxes and clear-sky domain fluxes, where only the surface albedo contributes to the upward fluxes. The range in the broadband radiative forcing under an overhead sun is over 80 W m^{-2} as a function of N_a, of which 55 W m^{-2} is from aerosol alone. At the larger SZA, the range in the broadband radiative forcing exceeds 200 W m^{-2}, with approximately 180 W m^{-2} of it contributed by the direct aerosol radiative forcing.

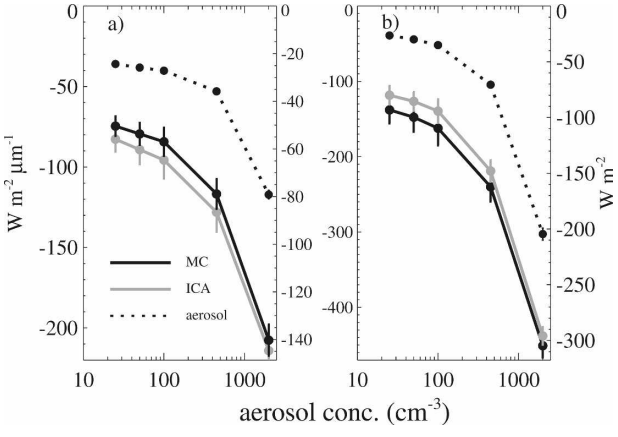

FIG. 4. The 0.64-μm spectral (left-hand axis) and shortwave broadband (right-hand axis) radiative forcing corresponding to Fig. 3.

Figure 5 shows the area-weighted cloud contribution to the albedo (still including the surface albedo). The standard deviations are 5%–10% of the mean values (more if the area-weighted surface albedo contribution is removed) indicating that variations in other variables besides aerosol can easily mask an increase in area-weighted cloud albedo from, for example, N_a = 25 to 100 cm^{-3}.

In these simulations, the cloud depth and horizontal dimensions decrease with increasing N_a (XF06). Except for the direct impact on the cloud fraction, the cloud morphological changes with N_a do not appear to influence the ICA–MC albedo differences, however. The ICA–MC albedo difference does not change much with N_a for the four cleaner cases, decreasing slightly at N_a = 2000 cm^{-3}. The lack of importance of cloud morphology is also captured by the gamma parameter $(\tau/\sigma_\tau)^2$, where σ_τ is the standard deviation in the cloud optical depth values (Barker 1996; Chambers et al. 1997a). High gamma parameter values are associated with increased 3DRT effects. The gamma parameter varies little with N_a in these simulations, even decreasing slightly for the highest N_a (not shown).

At the larger SZA, the MC–ICA difference decreases slightly more obviously with increasing N_a (Fig. 5b). The effective cloud area experiencing direct solar radiation is greater with a larger solar zenith angle than under an overhead sun because the cloud sides also

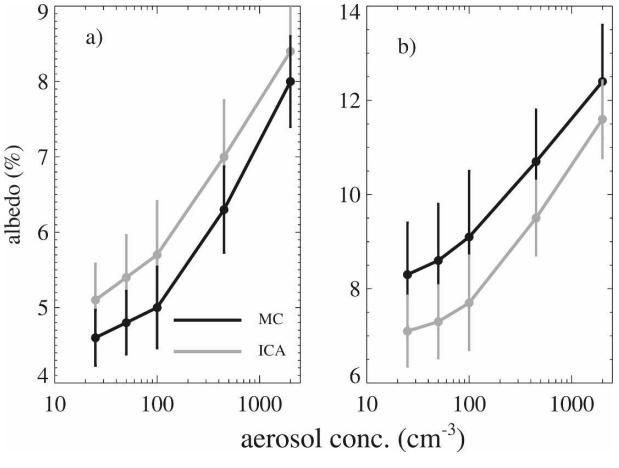

FIG. 5. The MC (black) and ICA (gray) domain-mean spectral albedo for the area-weighted cloudy regions only as a function of aerosol concentration for (a) overhead sun and (b) a SZA of 60° for the BOMEX simulations. Note the different scales in (a) and (b). A surface albedo of 0.03 is still included.

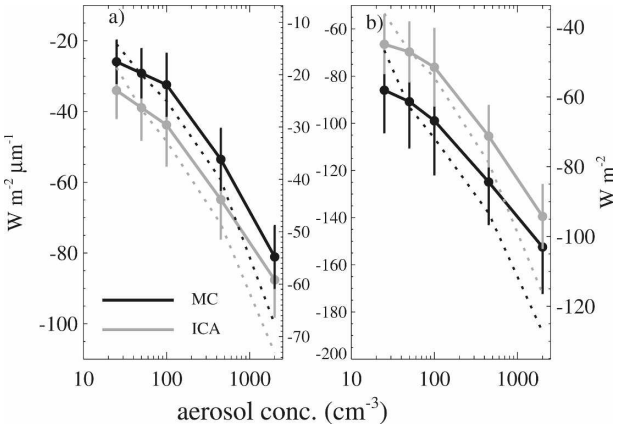

FIG. 6. The MC (black) and ICA (gray) 0.64-μm spectral (left-hand axis) and broadband (right-hand axis) CRF corresponding to Fig. 5. Dotted lines estimate the area-weighted CRF using the mean cloud fraction of all the simulations. Note the different scales for (a) and (b).

contribute. The decreasing cloud depth with N_a will contribute to a decreasing effective cloud area and may help compensate radiatively for the increasing cloud optical depth.

Figure 6 translates Fig. 5 into a top-of-domain spectral and broadband cloud radiative forcing (CRF). The increase in domain-mean cloud optical depth dominates the net radiative effect leading to an increased cooling. The changes in the broadband CRF for overhead sun as a function of N_a is about -8 W m^{-2} (100 cm^{-3})$^{-1}$ for the first 100 cm^{-3} increase in N_a decreasing in magnitude to -1.7 W m^{-3} (100 cm^{-3})$^{-1}$ for the last 1900 cm^{-3} change in N_a. At the greater SZA the same changes are slightly larger at -10 and -1.9 W m^{-2} (100 cm^{-3})$^{-1}$ increase in N_a, respectively. The 3DRT effects reduce the absolute magnitude of the broadband fluxes by approximately 10 W m^{-2} under overhead sun, a 20% relative reduction, and increase it by approximately 16 W m^{-2} when the sun is closer to the horizon, an approximate 20% relative increase.

The neglect of cloud fraction changes is illustrated in Fig. 6 as $\overline{\mathrm{CF}}F_{\mathrm{cld}}$, where $\overline{\mathrm{CF}}$ is the mean cloud fraction from all simulations (22.7%) and F_{cld} is the radiative forcing of only the cloudy pixels within each simulation. The reduction in cloud fraction with increasing N_a has a significant impact, reducing the area-weighted CRF under an overhead sun to approximately two-thirds from what it otherwise would be for these simulations, and by almost one-half at a solar zenith angle of 60°, both estimated from the changes in the radiative forcing between the cleanest and most polluted case. This result could depend on how cloud is defined; if most of the radiative forcing is from the optically thicker clouds, the area-weighted radiative forcing may be less sensitive to changes in cloud fraction (based on Fig. 1c). A more comprehensive evaluation at the greater solar zenith angle would also consider the effective cloud area using the "tilted independent pixel approximation" (Várnai and Davies 1999).

b. Susceptibility

Susceptibility evaluations have typically been applied analytically to overcast conditions (e.g., Feingold et al. 1997; Pincus and Baker 1994), relying on the two-stream approximation S_o. For the broken cloud fields evaluated within this study, the domain-mean susceptibility will differ from the cloud-only susceptibility because the cloud fraction also varies with N_a. We let $A_{\mathrm{dom}} = \mathrm{CF}A_{\mathrm{cld}}$ denote the area-weighted cloud albedo, so that

$$\frac{\partial A_{\mathrm{dom}}}{\partial N_d} = \overline{\mathrm{CF}}\,\frac{\partial A_{\mathrm{cld}}}{\partial N_d} + \overline{A_{\mathrm{cld}}}\,\frac{\partial \mathrm{CF}}{\partial N_d}, \tag{3}$$

with all other variables besides albedo and cloud fraction held constant and overlines indicating mean values from all five simulations. The results may be sensitive to the definition of cloud fraction (e.g., Charlson et al. 2007; Koren et al. 2007); we only evaluate results derived using a cloudy-column optical depth threshold of 0.001. The distinction between cloudy and clear sky is also more subjective at lower sun angles, when cloud sides also contribute to the effective cloud fraction seen by the sun, and for this reason the discussion is limited to the overhead sun case only. A susceptibility calculation requires that all other variables, in particular liquid water content, be held constant. This is approximated here by selecting scenes with mean cloud liquid water paths between 20 and 30 g m^{-2}, and again between 30 and 40 g m^{-2}. These thresholds were chosen because they allowed a sizable (8–22) number of cloud field realizations to participate from each N_a value (see also Fig. 1b).

The cloud susceptibilities, calculated directly from the MC and ICA cloud albedos, and by applying the more computationally efficient approximation S_o, calculated using Eq. (2), to both MC and ICA values, are shown in Fig. 7. The MC cloud susceptibilities are slightly less than those calculated from the ICA albedos, indicating that 3DRT effects tend to decrease the sensitivity of the cloud albedo to changes in droplet size. For the lower liquid water paths, the approximation S_o is clearly overestimating the actual cloud susceptibility, while for the higher liquid water paths, the approximation is adequate. Figure 7 cautions against applying S_o to clouds with low liquid water paths within

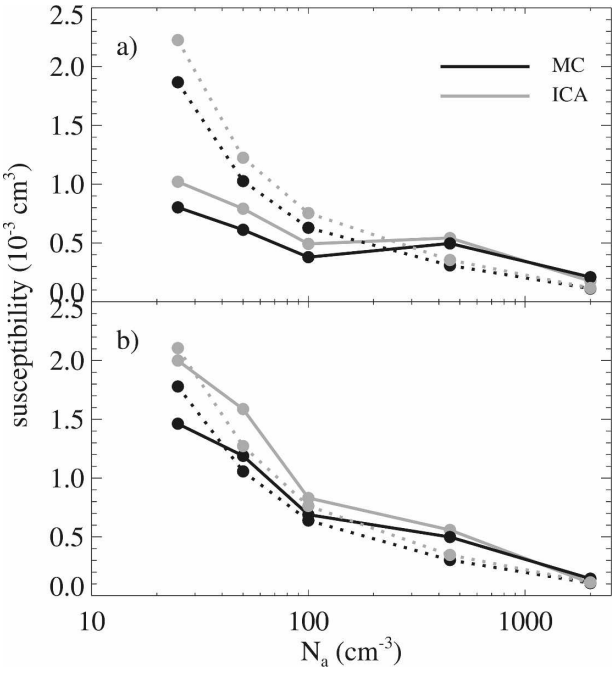

FIG. 7. The MC (black) and ICA (gray) ensemble-mean cloud susceptibility evaluated at 0.64 μm as a function of aerosol concentration for overhead sun, calculated using three-point differencing except at the endpoints, where the two-point difference from the neighboring value is shown. Black and gray dotted lines indicate the susceptibility approximation S_o as applied to the MC and ICA cloud albedos, respectively. Selected BOMEX scenes have mean cloud LWPs between 30 and 40 g m^{-3}.

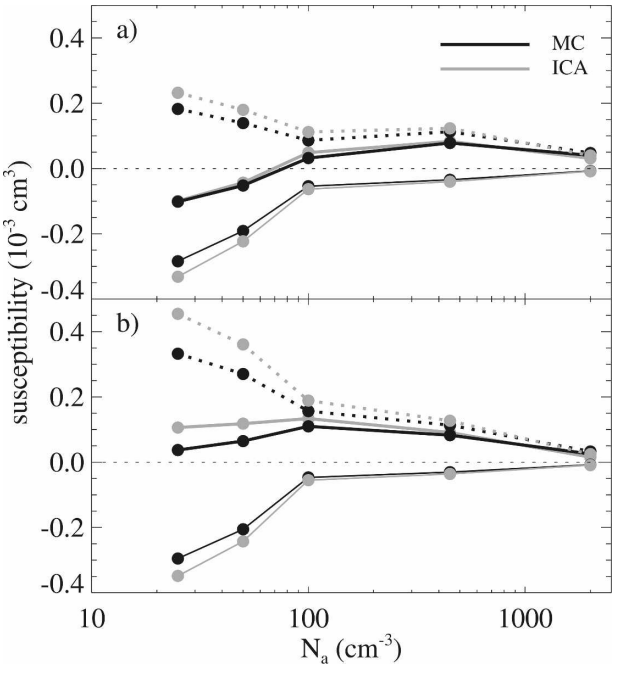

FIG. 8. The MC (black) and ICA (gray) area-weighted cloud susceptibility, evaluated at 0.64 μm, as a function of aerosol concentration for overhead sun. Dotted lines indicate the first term in Eq. (3), which is the cloud susceptibility weighted by the mean cloud fraction, and thin solid lines indicate the second term in Eq. (3), which is the change in cloud fraction weighted by the mean cloud susceptibility. Thick solid lines indicate the sum of these two terms. Selected BOMEX cloud fields have mean cloud LWPs between 30 and 40 g m^{-3}.

pristine aerosol conditions. The figure also suggests that for slightly thicker if broken clouds under an overhead sun, if the cloudy pixels (and N_d) can be identified successfully, that cloud susceptibilities estimated using S_o can provide good approximations of the true cloud susceptibility. At the larger solar zenith angle (not shown), the agreement is poor under more pristine conditions for both ranges of liquid water paths (where the susceptibility estimate holds more interest). The effective cloud area experiencing direct solar radiation needs to be considered within the susceptibility approximations to help improve the agreement at large solar zenith angles.

Figure 8 shows the area-weighted cloud susceptibility and the contribution of the two individual terms from Eq. (3) for the same cloud field realizations participating in Fig. 7. This evaluates separately the first (Twomey) aerosol indirect effect and the susceptibility associated with cloud fraction changes, again under an overhead sun. Both MC and ICA values are shown; these differ the most at low N_a values, with negative values even possible for clouds with LWPs $<$ 30 g m^{-2}, and are approximately equal to each other at $N_a > 100$ cm^{-3}. The highest area-weighted cloud susceptibility values now occur at intermediate (N_a = 100–500 cm^{-3}) aerosol concentrations. This contradicts the S_o prediction that cloud susceptibility is a maximum at the lowest droplet numbers, and comes about because the cloud fraction changes are also most pronounced at low droplet (aerosol) concentrations.

4. Results for cumulus beneath stratocumulus: ATEX simulations

The XFS07 simulations were constructed similarly to the XF06 simulations and are loosely based on Atlantic Trade Wind Experiment (ATEX) data. Simulations performed at aerosol concentrations of N_a = 25, 50, 100, 500 mg^{-1} are considered here. For simplicity, the aerosol residing between the clouds were not included in the radiative transfer calculations; this simplification is also justified by the relatively high cloud fractions (>70%). As might be expected based on Fig. 2, the mean area-weighted cloudy albedo initially increases almost linearly between N_a = 25 and 100 mg^{-1} (Fig. 9).

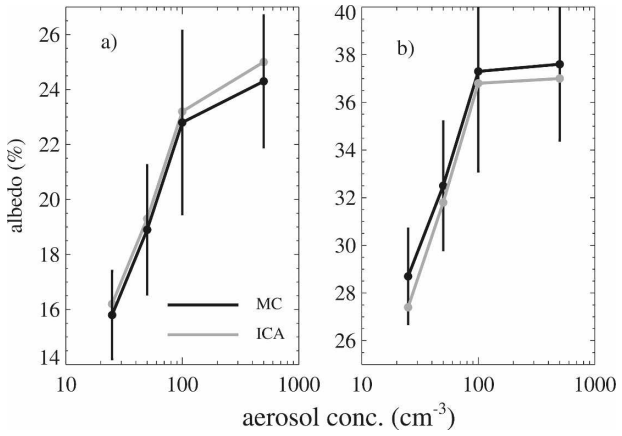

FIG. 9. The MC (black) and ICA (gray) domain-mean albedo for the area-weighted cloudy regions only, as a function of aerosol concentration for (a) overhead sun and (b) a SZA of 60° for the ATEX simulations. Note the different scales in (a) and (b). Direct aerosol radiative forcing is not included.

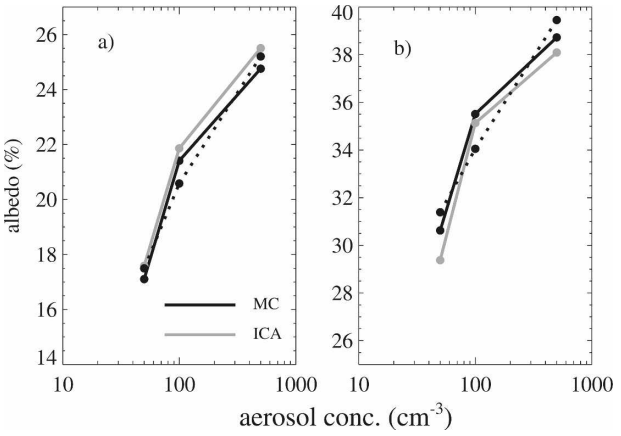

FIG. 10. The MC (black) and ICA (gray) domain-mean albedo for the area-weighted cloudy regions only, as a function of aerosol concentration for (a) overhead sun and (b) a SZA of 60° for the ATEX simulations. The black dotted lines indicate a domain-mean albedo estimate based on the mean cloud fraction of all the contributing simulations. Only those simulations with mean cloud LWPs between 55 and 65 g m^{-3} were selected. Note the different scales in (a) and (b).

This increase reflects contributions from both the aerosol-induced increase in cloud optical depth (even as the liquid water path decreases) as well as the increase in cloud fraction. Increased aerosol loading beyond N_a = 100 mg^{-1} has little impact upon the area-weighted cloudy albedo, however, because of two opposing effects: the increase in cloud optical depth is balanced by the decrease in (primarily stratiform) cloud fraction at the highest N_a. While 3DRT impacts are less for these simulations than for the BOMEX simulations, they are most pronounced at N_a = 500 mg^{-1}, which is when the optical depths are highest and the cloud cover is more broken.

The ATEX simulations do not lend themselves well to a susceptibility assessment as the cloud LWPs vary more strongly between the different aerosol concentrations (Fig. 2b). Nevertheless, a gauge can be made from the domain-mean albedo of cloud field realizations with mean cloud LWPs between 55 and 65 g m^{-3} (Fig. 10); approximately 15 such cloud field realizations exist each at N_a = 50, 100, 500 mg^{-1}. The Twomey aerosol indirect effect is apparent between N_a = 100 and 500 mg^{-1}, but the net radiative impact is reduced by the reductions in cloud coverage from that due to the Twomey effect alone (i.e., the difference in slope between the dotted and solid black lines). Between N_a = 50 and 100 mg^{-1} the opposite is true, with the radiative impacts from an increase in cloud coverage and the Twomey effect acting in concert.

5. Summary and discussion

The radiative impact of aerosol–cloud interactions, that is, the aerosol indirect effect, has been analyzed in two studies that illustrate the effects of both the microphysical responses, and the cloud fraction/distribution responses to changes in aerosol. Ultimately, it is the radiative impact that determines which of the many myriad aerosol effects on clouds is most important for radiative forcing and climate.

For the XF06 simulations, consisting of fields of broken trade wind cumulus with a mean cloud fraction of approximately 20% (depending on definition of cloud fraction), increased aerosol loading is associated with an increase in the domain-mean cloud optical depth despite decreasing domain-mean liquid water path, and the domain-mean cloudy albedo increases with N_a. The associated reduction in cloud coverage and cloud dimensions reduces the magnitude of the cooling by one-third to one-half from that attributable to the increased cloud optical depth alone (Fig. 6). This estimate is based on a comparison of $\overline{\mathrm{CF}}F_{\mathrm{cld}}$ to the actual radiative forcing at each N_a (Fig. 6) and may vary with how cloud fraction is defined.

The XFS07 simulations of stratiform cloud overlying cumulus have cloud fractions exceeding 70%. Aerosol loading is also associated with increases in cloud-only and domain-mean cloud optical depth despite large decreases in both the domain-mean and cloud liquid water path (Fig. 2). The XFS07 simulations contain two different scenarios, with differing effects on albedo: in the first, the cloud fraction increases with increasing aerosol and microphysical and macroscale responses act in unison to enhance the albedo; while, within the second, the responses counter one another in their im-

pact on the albedo. For the latter, the domain-mean cloudy albedo increased only slightly with aerosol loading beyond $N_a = 100\ \text{mg}^{-1}$ (Fig. 9), signifying a strong impact from the reductions in cloud fraction at higher N_a.

In both the XF06 and XFS07 simulations, the reductions in cloud fraction, attributed to a positive evaporation–entrainment feedback for the more polluted cases and smaller drop sizes, reduce the albedo significantly from that produced by the first or Twomey AIE alone. It is likely that such reductions in cloud fraction scale with cloud horizontal dimensions and cloud type. Mixing is challenging to represent. In these binned microphysics imulations, the mixing is homogeneous within the grid cell; that is, evaporation reduces the droplet sizes, with complete evaporation also reducing the total cloud droplet number concentration N_d. An inhomogeneous mixing process, where evaporation reduces the total N_d but the droplet sizes stay constant, will affect the radiation differently (e.g., Chosson et al. 2007). Larger-scale models require subgrid-scale mixing parameterizations (e.g., Grabowski 2007) that require development. Nevertheless, this study suggests that cloud parameterizations of the first AIE that do not simultaneously attempt to consider the influence of entrainment upon the cloud coverage, will produce erroneous estimates of the forcing attributable to aerosol–cloud interactions. The representation of these inherently small-scale processes poses significant challenges for climate models.

Our results contrast with those of McFarquhar et al. (2004), who found that soot-polluted clouds had a lower domain-mean cloud albedo than pristine clouds because the reduced cloud coverage more than offset the first AIE. The McFarquhar et al. (2004) study may reflect greater evaporation as a consequence of the solar absorption by soot or a weaker observed droplet size response to the changes in soot concentration (Heymsfield and McFarquhar 2001). Consistent with McFarquhar et al. (2004), the study of Jiang and Feingold (2006) showed that, in the case of absorbing aerosol, a nonmonotonic response of cloud optical depth to increases in aerosol is possible, as a result of the opposing effects of the first AIE and solar absorption by soot.

Three-dimensional radiative transfer effects were significant for the fluxes calculated from the XF06 simulations with their strongly broken cloud fields, altering the fluxes by 10%–20% from values calculated at the pixel level using plane-parallel radiative transfer theory (the ICA). Similarly strong 3DRT effects have been found within other modeling studies of broken shallow cumulus cloud fields over land (Pincus et al. 2005). In some observational studies, shallow tropical oceanic cumuli have been found to possess low cloud optical depths that do not necessarily produce significant 3DRT effects (Benner and Evans 2001; Chambers et al. 1997b), but the XF06 cloud optical depths, ranging up to 15 (Fig. 1d), are nevertheless representative of values reported over the tropical island of Nauru (McFarlane and Grabowski 2007). The 3DRT effects from cloud field anisotropy could conceivably vary significantly with N_a (Hinkelman et al. 2007) but were not considered. The XFS07 simulations of more homogeneous stratiform clouds did not demonstrate large 3DRT effects on their fluxes, consistent with other studies of this cloud type (e.g., Barker 1996; Zuidema and Evans 1998).

The cloud susceptibility, or the change in albedo with droplet concentration, was not strongly impacted by 3DRT effects under an overhead sun for the range of cloud LWPs examined (20–30 and 30–40 g m^{-2}) within the XF06 simulations. A popular two-stream radiative transfer approximation to the cloud susceptibility, S_o [Eq. (2)], did not apply well to the lower LWP clouds within pristine conditions, although it was found to closely approximate the cloud susceptibility for these clouds of small dimensions at the higher LWP (Fig. 7). A more comprehensive assessment using a larger range of solar zenith angles and taking the effective cloud area into account should be done, but these preliminary results suggest caution in applying the computationally inexpensive S_o calculation to satellite reflectance data such as from Clouds and the Earth's Radiant Energy System (CERES). Cloud susceptibility assessments using satellite reflectances may still remain most useful over (overcast) stratocumulus regions, where the adiabatic assumption can be applied to estimate the droplet number concentration N_d (e.g., Bennartz 2007).

Most previous modeling studies of cloud susceptibility have assumed overcast conditions; here we extended the evaluation for the XF06 simulations to also consider changes in cloud fraction. The contributions from cloud susceptibility and cloud fraction changes to a "domain" area-weighted cloud susceptibility were evaluated separately. The area-weighted susceptibility showed a strong sensitivity to the reductions in cloud fractions with increasing N_d, particularly at low droplet (or aerosol) concentrations where the cloud fractions were also changing the most rapidly. In the XF06 simulations, the cloud fraction changes modified the domain susceptibility such that the domain-mean albedo becomes most sensitive to modification by aerosol at an intermediate aerosol concentration, rather than under the cleanest conditions as traditionally expected. While not a general result, it does point to a potential nonmonotonicity

in susceptibility in situations where cloud fraction changes accompany aerosol-induced cloud albedo enhancements.

Large-eddy simulations (LES) possessing realistic feedbacks are particularly valuable for radiative studies. They provide a more confident understanding of the radiative field connection to the underlying cloud properties than is often possible with observed or retrieved cloud properties (e.g., Lane et al. 2002; McFarlane and Evans 2004; Zuidema et al. 2003). These LES simulations also help provide the bridge between discrepancies in climate model estimations of AIE radiative impacts and observed values. In this case, the ability of LES to resolve mixing (even as the details remain contested), a process that cannot be resolved by larger-scale models, coupled with a 3DRT calculation that is sensitive to the cloud morphology resulting from the mixing, allows for a unique assessment of a physical radiative impact on climate.

Acknowledgments. This study used the Bramley (July 2006) release of the I3RC Monte Carlo community model, developed by Robert Pincus with significant contributions from K. Franklin Evans (available online at http://i3rc.gsfc.nasa.gov/I3RC_community_model.htm). Support for this research from the NASA Radiation Sciences Program (Grant NNG04GF89G) is gratefully acknowledged by PZ. HX acknowledges support from a National Research Council postdoctoral fellowship and support from Chinese NSF Grant 40675004, while GF thanks NOAA's Climate Goal and NASA for support. Comments from Robert Pincus and two anonymous reviewers are appreciated and helped strengthen this study.

REFERENCES

Ackerman, A. S., O. B. Toon, D. E. Stevens, A. J. Heymsfield, V. Ramanathan, and E. J. Welton, 2000: Reduction of tropical cloudiness by soot. *Science,* **288,** 1042–1047.

Albrecht, B., 1989: Aerosols, cloud microphysics, and fractional cloudiness. *Science,* **245,** 1227–1230.

Barker, H. W., 1996: A parameterization for computing grid-averaged solar fluxes for inhomogeneous marine boundary layer clouds. Part I: Methodology and homogeneous biases. *J. Atmos. Sci.,* **53,** 2289–2303.

Bennartz, R., 2007: Global assessment of marine boundary layer cloud droplet number concentration from satellite. *J. Geophys. Res.,* **112,** D02201, doi:10.1029/2006JD007547.

Benner, T. C., and K. F. Evans, 2001: Three-dimensional solar radiative transfer in small tropical cumulus fields derived from high-resolution imagery. *J. Geophys. Res.,* **106,** 14 975–14 984.

Bohren, C. F., 1987: Multiple scattering of light and some of its observable consequences. *Amer. J. Phys.,* **55,** 524–533.

Cahalan, R. F., and Coauthors, 2005: The I3RC: Bringing together the most advanced radiative transfer codes for cloudy atmospheres. *Bull. Amer. Meteor. Soc.,* **86,** 1275–1293.

Chambers, L. H., B. A. Wielicki, and K. F. Evans, 1997a: Accuracy of the independent pixel approximation for satellite estimates of oceanic boundary layer cloud optical depth. *J. Geophys. Res.,* **102,** 1779–1794.

——, ——, and ——, 1997b: Independent pixel and two-dimensional estimates of Landsat-derived cloud field albedo. *J. Atmos. Sci.,* **54,** 1525–1532.

Charlson, R. J., S. E. Schwartz, J. M. Hales, R. D. Cess, J. A. Coakley Jr., J. E. Hansen, and D. J. Hofmann, 1992: Climate forcing by anthropogenic aerosols. *Science,* **255,** 423–430.

——, A. S. Ackerman, F. Bender, T. L. Anderson, and Z. Liu, 2007: On the climate forcing consequences of the albedo continuum between cloudy and clear air. *Tellus,* **59B,** 715–727.

Chosson, F., J.-L. Brenguier, and L. Schüller, 2007: Entrainment-mixing and radiative transfer simulation in boundary layer clouds. *J. Atmos. Sci.,* **64,** 2670–2682.

Feingold, G., R. Boers, B. Stevens, and W. R. Cotton, 1997: A modeling study of the effect of drizzle on cloud optical depth and susceptibility. *J. Geophys. Res.,* **102,** 13 527–13 534.

Genkova, I., G. Seiz, P. Zuidema, G. Zhao, and L. D. Di Girolamo, 2007: Cloud top height comparisons from ASTER, MISR, and MODIS for trade wind cumuli. *Remote Sens. Environ.,* **107,** 211–222.

Grabowski, W. W., 2007: Representation of turbulent mixing and buoyancy reversal in bulk cloud models. *J. Atmos. Sci.,* **64,** 3666–3680.

Han, Q., W. B. Rossow, J. Zeng, and R. Welch, 2002: Three different behaviors of liquid water path of water clouds in aerosol–cloud interactions. *J. Atmos. Sci.,* **59,** 726–735.

Heymsfield, A. J., and G. M. McFarquhar, 2001: Microphysics of INDOEX clean and polluted trade cumulus clouds. *J. Geophys. Res.,* **106,** 28 653–28 673.

Hinkelman, L. M., K. F. Evans, E. E. Clothiaux, T. P. Ackerman, and P. W. Stackhouse Jr., 2007: The effect of cumulus cloud field anisotropy on domain-averaged solar fluxes and atmospheric heating rates. *J. Atmos. Sci.,* **64,** 3499–3520.

Holland, J. Z., and E. M. Rasmusson, 1973: Measurements of the atmospheric mass, energy, and momentum budgets over a 500-kilometer square of tropical ocean. *Mon. Wea. Rev.,* **101,** 44–55.

Jiang, H., and G. Feingold, 2006: The effect of aerosol on warm convective clouds: Aerosol-cloud-surface flux feedbacks in a new coupled large eddy model. *J. Geophys. Res.,* **111,** D01202, doi:10.1029/2005JD006138.

——, H. Xue, A. Teller, G. Feingold, and Z. Levin, 2006: Aerosol effects on the lifetime of shallow cumulus. *Geophys. Res. Lett.,* **33,** L14806, doi:10.1029/2006GL026024.

Kaufman, Y. J., I. Koren, L. A. Remer, D. Rosenfeld, and Y. Rudich, 2005: The effect of smoke, dust, and pollution aerosol on shallow cloud development over the Atlantic Ocean. *Proc. Natl. Acad. Sci. USA,* **102,** 11 207–11 212.

Kiehl, J. T., and B. P. Briegleb, 1993: The relative roles of sulfate aerosols and greenhouse gases in climate forcing. *Science,* **260,** 311–314.

Kite, A., 1987: The albedo of broken cloud fields. *Quart. J. Roy. Meteor. Soc.,* **113,** 517–531.

Koren, I., L. A. Remer, Y. J. Kaufman, Y. Rudich, and J. V. Martins, 2007: On the twilight zone between clouds and aerosols. *Geophys. Res. Lett.,* **34,** L08805, doi:10.1029/2007GL029253.

Lane, D. E., K. Goris, and R. C. J. Somerville, 2002: Radiative

transfer through broken clouds: Observations and model validation. *J. Climate,* **15,** 2921–2933.

Lohmann, U., and J. Feichter, 2005: Global indirect aerosol effects: A review. *Atmos. Chem. Phys.,* **5,** 715–737.

Matheson, M. A., J. A. Coakley Jr., and W. R. Tahnk, 2005: Aerosol and cloud property relationships for summertime stratiform clouds in the northeastern Atlantic from Advanced Very High Resolution Radiometer observations. *J. Geophys. Res.,* **110,** D24204, doi:10.1029/2005JD006165.

Matsui, T., H. Masunaga, S. M. Kreidenweis, R. A. Pielke Sr., W.-K. Tao, M. Chin, and Y. J. Kaufman, 2006: Satellite-based assessment of marine low cloud variability associated with aerosol, atmospheric stability, and the diurnal cycle. *J. Geophys. Res.,* **111,** D17204, doi:10.1029/2005JD006097.

McFarlane, S. A., and K. F. Evans, 2004: Clouds and shortwave fluxes at Nauru. Part II: Shortwave flux closure. *J. Atmos. Sci.,* **61,** 2602–2615.

——, and W. W. Grabowski, 2007: Optical properties of shallow tropical cumuli derived from ARM ground-based remote sensing. *Geophys. Res. Lett.,* **34,** L06808, doi:10.1029/2006GL028767.

McFarquhar, G. M., S. Platnick, L. D. Di Girolamo, H. Wang, G. Wind, and G. Zhao, 2004: Trade wind cumuli statistics in clean and polluted air over the Indian Ocean from in situ and remote sensing measurements. *Geophys. Res. Lett.,* **31,** L21105, doi:10.1029/2004GL020412.

Norris, J. R., 1998: Low cloud type over the ocean from surface observations. Part II: Geographical and seasonal variations. *J. Climate,* **11,** 383–403.

——, 2001: Has northern Indian Ocean cloud cover changed due to increasing anthropogenic aerosol? *Geophys. Res. Lett.,* **28,** 3271–3274.

Pincus, R., and M. Baker, 1994: Effect of precipitation on the albedo susceptibility of clouds in the marine boundary layer. *Nature,* **372,** 250–252.

——, C. Hannay, and K. F. Evans, 2005: The accuracy of determining three-dimensional radiative transfer effects in cumulus clouds using ground-based profiling instruments. *J. Atmos. Sci.,* **62,** 2284–2293.

Platnick, S., and S. Twomey, 1994: Determining the susceptibility of cloud albedo to changes in droplet concentration with the Advanced Very High Resolution Radiometer. *J. Appl. Meteor.,* **33,** 334–347.

Rauber, R. M., and Coauthors, 2007: Rain in shallow cumulus over the ocean: The RICO campaign. *Bull. Amer. Meteor. Soc.,* **88,** 1912–1928.

Seinfeld, J. H., and S. N. Pandis, 1998: *Atmospheric Chemistry and Physics: From Air Pollution to Climate Change.* John Wiley and Sons, 1326 pp.

Siebesma, A. P., and Coauthors, 2003: A large eddy simulation intercomparison study of shallow cumulus convection. *J. Atmos. Sci.,* **60,** 1201–1219.

Stevens, B., C.-H. Moeng, and P. P. Sullivan, 1999: Large-eddy simulations of radiatively driven convection: Sensitivities to the representation of small scales. *J. Atmos. Sci.,* **56,** 3963–3984.

Várnai, T., 2000: Influence of three-dimensional radiative effects on the spatial distribution of shortwave cloud reflection. *J. Atmos. Sci.,* **57,** 216–229.

——, and R. Davies, 1999: Effects of cloud heterogeneities on shortwave radiation: Comparison of cloud-top variability and internal heterogeneity. *J. Atmos. Sci.,* **56,** 4206–4224.

Welch, R., and B. A. Wielicki, 1984: Stratocumulus cloud field reflected fluxes: The effect of cloud shape. *J. Atmos. Sci.,* **41,** 3085–3103.

Wen, G., A. Marshak, and R. F. Cahalan, 2006: Impact of 3-D clouds on clear-sky reflectance and aerosol retrieval in a biomass burning region of Brazil. *IEEE Geosci. Remote Sens. Lett.,* **3,** 169–172.

——, ——, ——, L. A. Remer, and R. G. Kleidman, 2007: 3-D aerosol-cloud radiative interaction observed in collocated MODIS and ASTER images of cumulus cloud fields. *J. Geophys. Res.,* **112,** D13204, doi:10.1029/2006JD008267.

Wielicki, B. A., and L. Parker, 1992: On the determination of cloud cover from satellite sensors: The effect of sensor spatial resolution. *J. Geophys. Res.,* **97,** 12 799–12 823.

Xue, H., and G. Feingold, 2006: Large-eddy simulations of trade wind cumuli: Investigation of aerosol indirect effects. *J. Atmos. Sci.,* **63,** 1605–1622.

——, ——, and B. Stevens, 2007: Aerosol effects on clouds, precipitation, and the organization of shallow cumulus convection. *J. Atmos. Sci.,* **65,** 392–406.

Zhao, G., and L. D. Di Girolamo, 2006: Cloud fraction errors for trade wind cumuli from EOS-Terra instruments. *Geophys. Res. Lett.,* **33,** L20802, doi:10.1029/2006GL027088.

——, and ——, 2007: Statistics on the macrophysical properties of trade wind cumuli over the tropical western Atlantic. *J. Geophys. Res.,* **112,** D10204, doi:10.1029/2006JD007371.

Zuidema, P., and K. F. Evans, 1998: On the validity of the independent pixel approximation for boundary layer clouds observed during ASTEX. *J. Geophys. Res.,* **103,** 6059–6074.

——, R. Davies, and C. Moroney, 2003: On the angular radiance closure of tropical cumulus congestus clouds observed by the Multiangle Imaging Spectroradiometer. *J. Geophys. Res.,* **108,** 4626, doi:10.1029/2003JD003401.